

# Numerical Study of Focused Wave Interactions with a Single-Point Moored Hemispherical-Bottomed Buoy

Zhenghao Liu, Yuan Zhuang and Decheng Wan\*

Computational Marine Hydrodynamics Lab (CMHL), State Key Lab of Ocean Engineering, School of Naval Architecture, Ocean and Civil Engineering, Shanghai Jiao Tong University, Shanghai, China

**In this work, our computational fluid dynamics (CFD) solver naoe-FOAM-SJTU is adopted to simulate the interaction between focused waves and a moored hemispherical-bottomed buoy. This solver adopts a two-phase Navier–Stokes model and a spring mooring system. Three crest-focused wave groups, based on NewWave theory, are generated and validated against the experimental measurements from the Collaborative Computational Project in Wave–Structure Interaction (CCP-WSI) working group. Numerical results for the buoy’s heave and surge displacement, pitch angle, and mooring load are compared against corresponding physical data. The effects of wave steepness on the behavior and mooring loads are discussed.**

## INTRODUCTION

Under extreme wave conditions, strong nonlinear impact phenomena such as severe wave runup, relative motion, and green water may occur, which will cause a large local impact load on wave energy converters (WECs). Exploring the interaction between extreme waves and WECs has great importance for the design and protection of these kinds of structures. As an extreme wave is highly nonlinear and can arise as a highly transient event within a multifrequency sea state, a focused wave group is typically adopted to model an extreme wave in physical or numerical modeling. The focused wave group where many wave components in a spectrum focus simultaneously at a position in space can represent an extreme wave profile with a specified wave energy spectrum. Thus, a focused wave can play the role for extreme wave conditions. The accurate prediction of the motion of a WEC under extreme wave conditions can be viewed as that under the focusing wave.

Previously, Savin et al. (2012) experimentally measured lateral force acting on the funnel under two sea states. Two measurements were taken by two separate measuring systems with slightly different timing. The development of the method could be used for evaluation of the forces from waves acting on the WEC. Azimuth-inclination angles and snatch load on a tight mooring system are mainly discussed in their work. Hann et al. (2015) considered experimental measurements of the interaction of a taut moored floating body, representing a WEC in survivability mode, with extreme waves. They discussed the influence of wave steepness effect on model response and mooring load using focused wave groups. Goteman et al. (2015) considered the survivability of a 1:20 scale point-absorbing WEC model in extreme wave tests with focused waves embedded in regular waves and irregular waves. Mai et al. (2016) performed experiments to examine

wave–structure interactions for a series of simplified floating production storage and offloading (FPSO)-shaped bodies.

Besides experimental investigation of wave interaction with floating structures, numerical methods have also been widely used in dealing with this problem. Wolgamot and Fitzgerald (2015) reviewed efforts that have been made to analyze the behavior and performance of WECs using nonlinear hydrodynamics methods. They affirmed the potential advantages of solving the wave–structure interaction problems by computational fluid dynamics (CFD) methods. Sykes et al. (2009) provided a preliminary assessment of the validity of employing a boundary element method (BEM) code to predict the displacement and associated hydrodynamic forces of a simple floating oscillating water column (OWC). Bredmose and Jacobsen (2010) computed breaking wave loads on a monopile foundation within a three-dimensional CFD model. The wave impacts were obtained by application of focused wave groups to the amplitudes of a Joint North Sea Wave Project (JONSWAP) spectrum. The CFD results were compared to load estimations obtained from the Morison equation. Westphalen (2011) applied two commercial Navier–Stokes solvers to solve wave–wave and wave–structure interaction problems for the final application of simulating a single float of the WEC. Li and Lin (2012) studied fully nonlinear wave–body interactions for a stationary floating structure under regular and irregular waves for different water depths, wave heights, and periods in a two-dimensional numerical wave tank. Palm et al. (2013) used open-source code OpenFOAM to simulate the dynamics of a floating WEC coupled to a high-order finite element solver for cable dynamics. Their results illustrated that the coupled model is able to capture the complicated force propagation in the mooring cables. They numerically simulated a moored floating vertical cylinder in six degrees of freedom (6DoF) based on OpenFOAM (Palm et al., 2016). Then, Palm et al. (2018) analyzed the nonlinear forces on a moored point-absorbing WEC in resonance at prototype scale and at model scale. They recommended that both Reynolds-averaged Navier–Stokes (RANS) equations and Euler simulations could be used during numerical validation against experimental model scale tests in order to separate the viscous drag influence from the induced drag. Consequently, this approach could be used to quantify the effects of scale on WECs. Ransley (2015) used a numerical tool based on OpenFOAM to simulate focused wave impacts on generic WEC hull forms. Two floating

\*ISOPE Member, Corresponding Author.

Received August 17, 2019; updated and further revised manuscript received by the editors December 16, 2019. The original version (prior to the final updated and revised manuscript) was presented at the Twenty-ninth International Ocean and Polar Engineering Conference (ISOPE-2019), Honolulu, Hawaii, June 16–21, 2019.

KEY WORDS: Wave–structure interactions, naoe-FOAM-SJTU solver, focused wave, 6DoF motion, mooring loads.

structures, a fixed truncated surface-piercing cylinder and a floating hemispherical-bottomed buoy with a linear spring mooring, were simulated. The results have been validated against the experimental data. They also discussed the development of a numerical wave tank and its capability of simulating the coupled behavior of WECs and the moorings under extreme wave loading. Bharath et al. (2016) applied a nonlinear, viscous volume of a fluid RANS model to simulate the diffraction and radiation for a single heaving submerged spherical WEC. Wagner et al. (2016) performed hydrodynamic analysis of oscillation of a submerged plate WEC under nonlinear shallow water waves. Lou (2017) studied the coupled fluid–structure interaction (FSI) of a WEC and evaluated the design of a WEC mooring system. Lim et al. (2018) carried out prediction of the long-term extreme response of a simple moored floating offshore structure using polynomial chaos expansion.

All methods mentioned above can predict the loading and dynamic response of WECs in large nonlinear waves (Coe and Neary, 2014). Well-targeted validation work has the potential to better determine which of these methods is best suited to each stage of a WEC survival analysis. Therefore, a systematic approach must be employed to the survival aspect of WEC design.

The present work is part of a comparative study on focused wave interactions with floating structures, the Collaborative Computational Project in Wave–Structure Interaction (CCP-WSI) Blind Test Series 3. The objective of the present work is to investigate the interaction between focused waves and a hemispherical-bottomed buoy. In this paper, present CFD calculations are performed by the CFD solver naoe-FOAM-SJTU. (The abbreviation “naoe” stands for “naval architecture and ocean engineering.”) The time histories of focused waves at target locations were compared with the experimental data provided by the CCP-WSI working group. The results show that the current approach can be an alternative tool to generate focused waves according to the experiment. The free-surface elevation in the vicinity of the structure is captured by several wave gauges. The effects of wave steepness on the motion of the floating structure and the mooring load are presented and discussed. Under our present CFD solver, the floating structure with a mooring system through a nonlinear wave can be solved and analyzed accurately.

## NUMERICAL METHODS

### Governing Equations

Based on the open-source platform OpenFOAM, the CFD solver naoe-FOAM-SJTU is designed for computing viscous flows around ocean structures (Wang et al., 2016; Zhao and Wan, 2016; Wang and Wan, 2018; Zhao et al., 2018). Compared to the OpenFOAM standard solver, the naoe-FOAM-SJTU solver is complemented with a wave generation and damping module, a wave probe module, a 6DoF motion module, a mooring system module, turbulence models, and an overset module. The governing equations of incompressible viscous fluids in naoe-FOAM-SJTU solver are as follows:

$$\nabla \cdot U = 0 \quad (1)$$

$$\frac{\partial \rho U}{\partial t} + \nabla \cdot (\rho(U - U_g)U) = -\nabla p_d - g \cdot x \nabla \rho + \nabla \cdot (\mu_{\text{eff}} \nabla U) + (\nabla U) \cdot \nabla \mu_{\text{eff}} + f_\sigma + f_s \quad (2)$$

where  $U$  and  $U_g$  are the velocity field and the velocity of grid nodes, respectively.  $p_d$  is the dynamic pressure,  $p$  is the total pressure, and  $\rho$  is the mixed density of the two phases water and air.  $\mu_{\text{eff}}$  is the effective dynamic viscosity in which  $\nu$  and

$\nu_t$  are kinematic viscosity and eddy viscosity, respectively.  $f_\sigma$  is the surface tension, which impacts the free surface.  $f_s$  is a source term, added to generate the sponge layer for wave absorbing.

### Numerical Wave Tank

The numerical simulations in this work are performed in a numerical wave tank based on the naoe-FOAM-SJTU solver. The volume-of-fluid (VOF) method (Hirt and Nichols, 1981) with artificial bounded compression techniques is adopted to capture the free surface. Three wave-making modules, including piston-type wave maker, flap-type wave maker, and velocity inlet, are extended to the naoe-FOAM-SJTU solver (Shen et al., 2015; Wang et al., 2015; Wang and Wan, 2016). The velocity inlet (Dirichlet boundary condition) is adopted to generate the focused waves according to the existing wave theory in this work. In the numerical wave tank, each focused wave can be created using a linear superposition of 244 wave fronts with frequencies evenly spaced between 0.101563 Hz and 2 Hz and a theoretical focus location. The amplitudes of the frequency components were derived by applying the NewWave theory to a Pierson–Moskowitz or JONSWAP spectrum. To avoid wave reflection, a sponge layer is set up at the outlet of the computational domain by adding a source term  $f_s$  into Eq. 2.

### Dynamic Deformation and Overset Grid Technology

In this study, both dynamic deformation and overset grid technique are applied to deal with the buoy motion. For the dynamic deformation mesh, the mesh velocity is determined by solving Laplace’s equation at each time step, and the new positions of the vertices of the mesh can therefore be obtained as follows:

$$\nabla \cdot (\gamma \nabla U_g) = 0 \quad (3)$$

where  $\gamma = 1/r^2$  is the quadratic inverse distance of cell center to the nearest moving wall boundary and  $U_g$  is the grid velocity. While using the overset grid technique, the decomposed overlapping grids for each part with independent movement are allowed, which makes it powerful for simulating large-amplitude motion problems. Additionally, the information transformation between each grid domain is built by interpolation at appropriate cells or points using domain connectivity information (DCI), which is produced by Suggar++. Detailed information about these two grid technologies can be found in Wang et al. (2019).

### Mooring System

In order to model the mooring system in the CFD simulation, an equivalent spring system for 6DoF motion is implemented to the naoe-FOAM-SJTU solver. The mooring system in the present solver consists of several mooring lines. Each mooring line is anchored to a fixed point at one end and attached to the moving body at the other end. The solution procedure of the mooring system is summarized as follows: compute mooring forces and moments and add them as external excitation to the rigid body motion equations, solve the 6DoF motion equations and update motion state for the rigid body, and update the mooring line shape for the current time step and go to the next time step. The motion can be modeled by means of a mass-spring damping system. The natural frequency of this mass-spring system can be given as

$$f_n = \frac{1}{2\pi} \sqrt{\frac{k}{m + \Delta m}} \quad (4)$$

where  $k$  is the equivalent stiffness of the mass-spring system,  $m$  is the mass of the WEC, and  $\Delta m$  is the added mass of the WEC submerged in water. For natural rotation frequency, it can be described as

$$f_{nt} = \frac{1}{2\pi} \sqrt{\frac{k_t}{J + J_a}} \quad (5)$$

where  $k_t$  is the equivalent rotation stiffness of the mass-spring system,  $J$  is the moment of inertia of the WEC, and  $J_a$  is the added moment of inertia of the WEC submerged in water. Each spring line can be defined by four physical parameters: pretension, stiffness, anchor, and fairlead.

### NewWave Theory

In offshore engineering, a designed wave known as NewWave can be used to represent the profile of extreme waves. NewWave relies on the dispersive nature of water waves to produce an extreme wave event at a specific point in space and time by combining smaller, sinusoidal components of different frequencies. Retaining the broad-banded nature of extreme ocean waves, the linear NewWave has a shape based on the average extreme in a linear, random, Gaussian sea and is proportional to the auto-correlation function (the Fourier transform of the sea-state power spectrum in question). By discretizing this definition into a finite number of sinusoidal components,  $N$ , and by limiting ourselves to unidirectional seas, a linear crest-focused wave group then has the surface elevation

$$\eta(x, t) = \sum_{n=0}^N a_n \cos(k_n(x - x_f) - \omega_n(t - t_f)), \quad (6)$$

where  $x_f$  and  $t_f$  are the target position and target time, respectively. For a linear NewWave, the individual component amplitudes are given by

$$a_n = \frac{A_{cr} S_n(\omega) \Delta\omega_n}{\sum_n S_n(\omega) \Delta\omega_n}, \quad (7)$$

where  $S_n(\omega)$  is the energy spectrum,  $\Delta\omega_n$  is the frequency increment, and  $A_{cr}$  is the linear crest amplitude given by

$$A_{cr} = \sqrt{2m_0 \ln(N)} \quad (8)$$

where  $m_0$  is the zeroth moment of the spectrum, and  $N$  is the number of wave components. A JONSWAP spectrum is assumed when applying NewWave theory:

$$S(\omega) = 319.34 \frac{h_{1/3}^2}{T_p^4 \omega^5} \exp\left[-\frac{1948}{(T_p \omega)^4}\right] 3.3 \exp\left[\frac{-(0.159 T_p \omega - 1)^2}{2\sigma^2}\right] \quad (9)$$

where  $h_{1/3}$  is the significant wave height and  $T_p$  is the peak wave period.

### Discretization Schemes

The finite volume method (FVM) is adopted to discretize the RANS and VOF transport equations in OpenFOAM. A Van Leer scheme is applied for the VOF equation. The merged PISO-SIMPLE (pressure-implicit with splitting of operators, semi-implicit method for pressure linked equations) algorithm is used to solve the coupled equation of velocity and pressure. The convection terms are solved by a second-order total variation diminishing (TVD) limited linear scheme, and the diffusion terms are approximated by a second-order central difference scheme.

## GEOMETRY AND TEST CONDITIONS

### Experimental Setup

The present work is part of the comparative study on focused wave interactions with floating structures. The physical experiments were performed in the COAST Laboratory Ocean Basin at Plymouth University, UK. The wave tank is 35 m × 15.5 m and has 24 flap-type, force feedback-controlled wave makers with a hinge depth of 2 m. The water depth at the wave makers is 4 m with a linear slope to the working area, which is 3.0 m deep. The detailed description of a parabolic absorbing beach at the end of the tank and the layout of 13 wave gauges in the physical tank are illustrated in Ransley et al. (2017).

### Model Geometry

A hemispherical-bottomed buoy with the radius of the hemisphere and the cylinder equal to 0.25 m is placed at wave gauge 5. The height of the cylindrical section is also 0.25 m. The overall height of the buoy is 0.5 m. The draft of the buoy is 0.322 m and  $z$  position of center of mass (CoM) is -0.141 m. The mass of the buoy is 43.67 kg. The moment of inertia about the  $x$ ,  $y$ ,  $z$  axis is 1.620, 1.620, and 1.143 kgm<sup>2</sup>, respectively. Figure 1 shows the physical model in both experimental and numerical simulations. The mooring attachment is located at the bottom-most point of the hemisphere on the axial line. The mooring used is a linear spring with a stiffness of 67 N/m and a rest length of 2.224 m. The pretension in the mooring is 32.07 N.

### Test Conditions

The crest-focused waves are generated based on a NewWave theory. Table 1 shows the wave parameters for both the empty wave tank simulation case and the floating buoy case:  $An$  is the main crest amplitude,  $fp$  is the peak frequency,  $h$  is the water depth,  $Hs$  is the significant wave height, and  $kA$  is the wave steepness, where  $k$  is the wave number. Those three cases have different wave steepnesses. Each wave was created by COAST using a linear superposition of 244 wave fronts with frequencies evenly spaced between 0.101563 Hz and 2 Hz and a theoretical focus location  $x = 14.8$  m from the wave generation boundary. The wave frequencies, wave amplitudes, and phase angles were

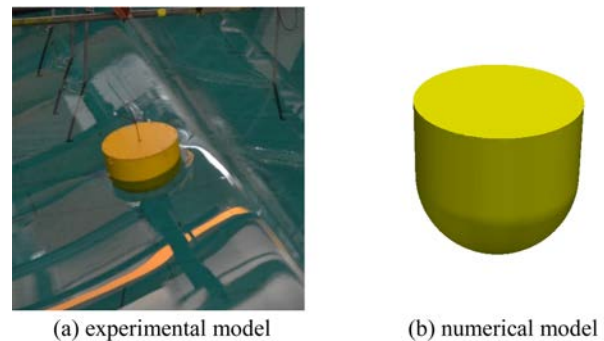


Fig. 1 Geometry of the physical model

CCP-WSI ID	$An$ (m)	$fp$ (Hz)	$h$ (m)	$Hs$ (m)	$kA$
1BT3	0.2	0.4	3.0	0.274	0.128778
2BT3	0.3	0.4	3.0	0.274	0.193167
3BT3	0.32	0.4	3.0	0.274	0.206044

Table 1 Wave parameters for each test

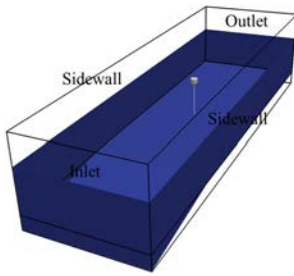


Fig. 2 Computational domain

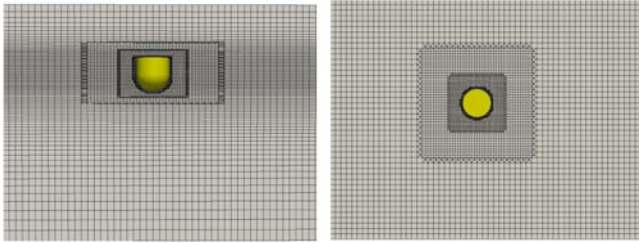


Fig. 3 Computational mesh around the hemispherical-bottomed buoy

derived by means of a fast Fourier transform (FFT) of the time series recorded at the upstream wave gauge during the physical experiments.

### Numerical Models

Using the CFD solver naoe-FOAM-SJTU, the focused wave is simulated with and without the floating hemispherical-bottomed buoy, respectively. According to the physical experiment, the numerical domain was set to  $0 < x < 27$  m,  $-4$  m  $< y < 4$  m,  $-4$  m  $< z < 2$  m. The computational domain is shown in Fig. 2. Figure 3 shows the computational mesh around the hemispherical-bottomed buoy. The total grid number is approximately 2.31 million for the empty tank and 2.97 million for the case with the buoy, respectively. The mesh generation is selected according to the grid convergence study in the next section. The wave generation boundary is located at  $x = 0$  m. The hemispherical-bottomed buoy is placed at  $x = 14.8$  m. The boundary conditions are set as follows: the velocity inlet boundary condition is adopted, the zero-gradient condition is applied at the outlet, the slip boundary condition is considered at the bottom and at side boundaries, and the nonslip boundary condition is set at the buoy surface. The turbulence model is chosen as laminar. The time step is 0.002 s for each case. All computations are conducted via high-performance computing (HPC). The HPC processor is the Intel Xeon E5-2670 (8 Cores, 2.6 GHz, 20 MB Cache, 8.0 GT). The number of processors for each case is 56. For the empty wave tank case, the CPU time for specified time range (35.3–50.3 s) is approximately 22.3 h. For the wave–buoy interaction case, the CPU time for the specified time range (35.3–50.3 s) is approximately 25.3 h.

## RESULTS AND DISCUSSION

### Grid Convergence Study

First, a grid convergence study is carried out to validate the accuracy of the wave generation of the current numerical model. For case 1BT3, three different meshes are adopted in a grid convergence study. The total grid number of coarse mesh, medium

mesh, and fine mesh is 1.75 million, 2.31 million, and 3.52 million, respectively. The time step is 0.002 s in each case. As the grid is refined, the focused wave amplitude approaches the experimental data monotonically. The wave amplitude of the medium mesh shows little difference from the fine mesh case, as shown in Fig. 4b. The error of focused wave amplitude between the medium mesh and experimental data is within 3.5%. In order to quantitatively estimate uncertainty due to grid and time step errors, we adopt a verification method proposed by Stern et al. (2006). The convergence solution ( $R_G$ ) of different solutions ( $S_i$ ) is defined as

$$R_G = \frac{S_2 - S_1}{S_3 - S_2} \quad (10)$$

where  $S_i$  corresponds to solutions with fine, medium, and coarse mesh, respectively. Additionally, different  $R_G$  values represent different convergence conditions: (1)  $0 < R_G < 1$  represents monotonic convergence, and generalized Richardson extrapolation (RE) is used to estimate grid uncertainty; (2)  $R_G < 0$  represents oscillatory convergence, and uncertainties can be estimated by attempting to bound the error based on oscillation maximums  $S_U$  and minimums  $S_L$ ; (3)  $R_G > 1$  represents divergence, and uncertainties cannot be estimated. In our study, the results show good convergence, as summarized in Table 2. As the grid is refined, the maximum crest of wave elevation approaches the experimental data monotonically. Thus, the RE method is used to estimate convergence rate in this study (Roache, 1994). Order of discretization is estimated as follows:

$$P = \frac{\ln(1/R_G)}{\ln(r)} \quad (11)$$

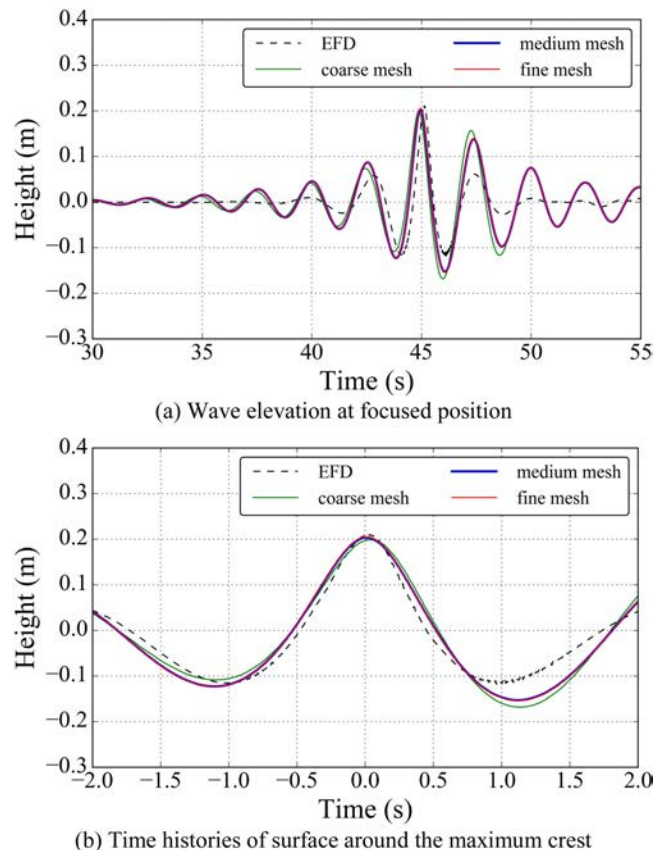


Fig. 4 Wave elevation at focused position for different grid numbers

Grid	ID	Grid Size	Wave Height	Error of Wave Height
EFD			0.210m	
Fine	S1	3.52M	0.205 m	-2.38%
Medium	S2	2.31M	0.203 m	-3.33%
Coarse	S3	1.75M	0.197 m	-6.19%
$R_G$			0.333	
$P$			3.265	
$GCI_{12}$			0.59%	
$GCI_{23}$			1.78%	
Convergence type			Monotonic	

Table 2 Grid convergence study for case 1BT3

Then, the grid convergence index (GCI) is defined:

$$GCI_{ij} = F_S \frac{|e_{ij}|}{r^p - 1} \quad (12)$$

where  $F_S$  is a safety factor. For a convergence study with a minimum of three grids or more,  $F_S = 1.25$ , according to Roache (1994).  $e_{ij}$  is the error between  $S_i$  and  $S_j$ . The GCI can indicate the error using different grids. A small GCI means that the solution is relatively accurate. Table 2 shows the GCI values of wave elevation at a focused location. The maximum crest of wave elevation shows monotonic convergence with  $R_G$  of 0.333. The  $GCI_{12}$  (between fine and medium) of the maximum crest is only 0.59%, which can illustrate that grid density has a limited effect on maximum wave crest at a focused location in fine and medium mesh grid. It is obvious that the values of  $GCI_{23}$  (between medium and coarse) are larger than those of  $GCI_{12}$  and that the error of the maximum wave crest between the coarse mesh grid and experimental results is much larger than that of the medium and fine mesh grid. The grid uncertainty between the simulation results of fine mesh grid and medium mesh grid is under 1%, but the computational time is significantly increased. The medium mesh grid is selected in our study.

### Wave Elevation in Empty Wave Tank

To validate wave generation and propagation, the numerical results are compared with the experimental data provided by CCP-WSI. The time histories of wave elevations are presented in Figs. 5–7. These are from several wave gauges along the wave tank in three cases. The time history of the free-surface elevation

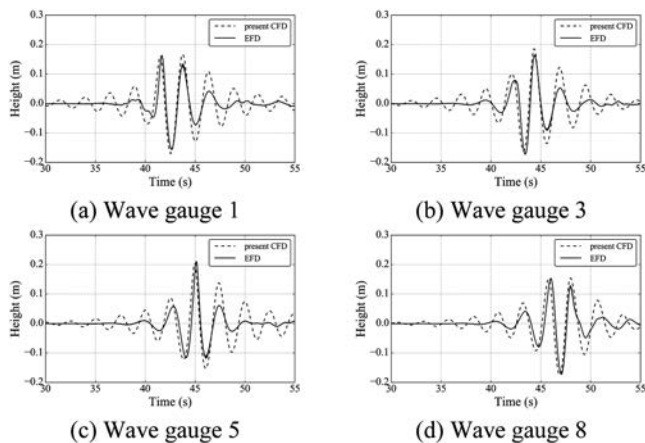


Fig. 5 Wave elevation at different wave gauges for case 1BT3

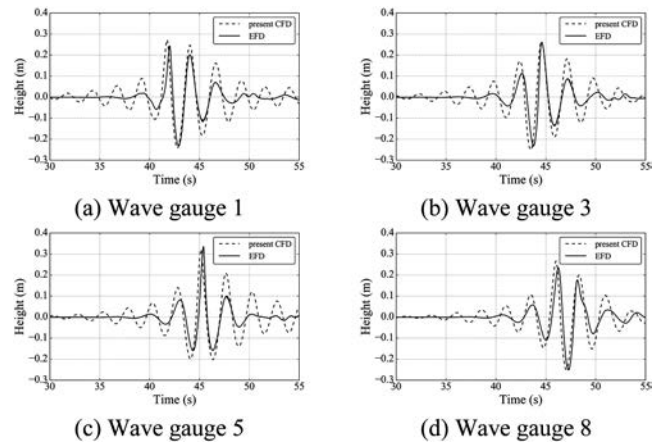


Fig. 6 Wave elevation at different wave gauges for case 2BT3

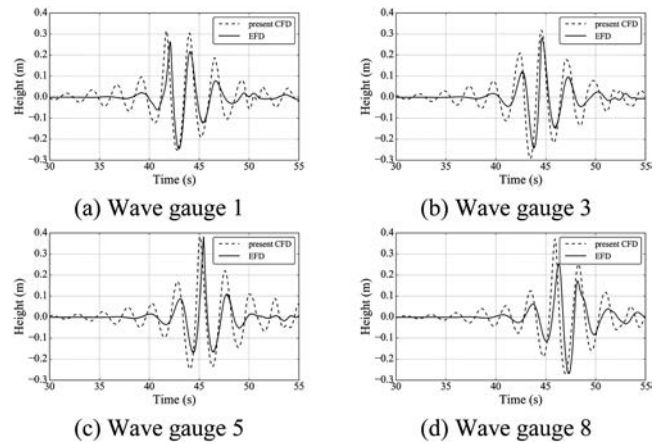


Fig. 7 Wave elevation at different wave gauges for case 3BT3

at the focused location ( $x = 14.8$  m) without the hemispherical-bottomed buoy is investigated. As can be seen in Figs. 5–7, the numerical results show good agreement with the experimental data, especially at the focused location  $x = 14.8$  m (in Figs. 5c–7c). A sharp wave crest can be found at the focused time in both the experiment and numerical simulations. After the focused time, the amplitude of the surface elevation decreases as the energy content of the wave decreases. Moreover, as shown in Figs. 5–7, with the increase of the wave steepness, the nonlinearity of the focused wave is more obvious. The focused wave crest of case 3BT3 is sharper than the other two cases. The wave amplitude at wave gauge 5 is within 3.5% of the experimental value for the three cases. For all wave gauges, the numerical results of the wave elevation after the focused time are larger than the experimental data. This may be a result of different wave generation methods between the experiment and numerical simulation. However, the wave crests considered at the focused time are almost consistent with the experiment. For case 1BT3, the wave trough at the focused location and time shows reasonable agreement with the experimental results, while for the other two cases, our numerical results present additional energy compared to the experimental results. It can be also observed that the main crests at some wave gauges (e.g., wave gauge 3) are larger than the experimental results. This is more obvious for the steeper wave case. Additionally, the oscillation of the surface before and after the largest crest is more evident than the experimental results. This may be caused by the effect of the oblique bottom of the wave tank. A new wave generation method and boundary condition should be used in fur-

ther work. The waves will be generated by an expression-based boundary condition formed from the linear superposition of wave components derived using an FFT of the surface elevation at wave gauge 1 in the empty tank test.

**Wave Interaction Between Focused Waves and Hemispherical-Bottomed Buoy**

To analyze the buoy’s motion response, the dynamic deformation grid coupled with the 6DoF module and the overset grid coupled with the 6DoF module are adopted in this work. The time histories of surge, heave, and pitch motion are presented and compared with the experimental results in Figs. 8–10, respectively. In these figures, the original CFD represents the numerical results by dynamic deformation grid, and the modified CFD represents the results calculated by overset grid. Here, we present the modified results only for case 1BT3. As can be seen in Figs. 8a–10a and in Figs. 8c–10c, the heave and pitch motion of the buoy can be captured relatively well compared to the experimental results. For case 1BT3, the modified CFD shows great improvement in the prediction of buoy motion and mooring loads. Therefore, we will use the modified CFD results for case 1BT3 in the discussion. For the heave motion, the error of the CFD and EFD results at the focused time is  $-10.91%$ ,  $-15.27%$ , and  $-20.51%$ , respectively. The prediction accuracy decreases as the wave steepness increases. For the pitch motion, the error of the CFD and EFD results at the focused time is  $-6.71%$ ,  $-13.92%$ , and  $-10.89%$ , respectively. For mooring loads, the error of the CFD and EFD results at the focused time is  $-2.46%$ ,  $-4.78%$ , and  $+1.14%$ , respectively. This indicates that our solver performs well even for large body motion. As for surge motion, although none of the cases present good agreement with the experimental results, the long-period surge oscillation still can be captured in our numerical simulations. The surge displacement of the buoy can reach one diameter or more of the buoy in the 2BT3 and 3BT3 cases. Generally, the motion in surge, heave, and pitch increases with the increasing wave steepness, as shown in Figs. 8–10.

**The Effect of Wave Steepness on Buoy Motion Response**

Figure 11 shows the time history of the motion response of the buoy under different wave steepnesses. For the heave and pitch motion, it can be seen that, as the wave steepness increases, the amplitude of the heave motion also increases. The increased amplitude of heave and pitch motion is proportional to the increased amplitude of the focused waves. The increase in wave steepness not only changed the amplitude of the buoy motion

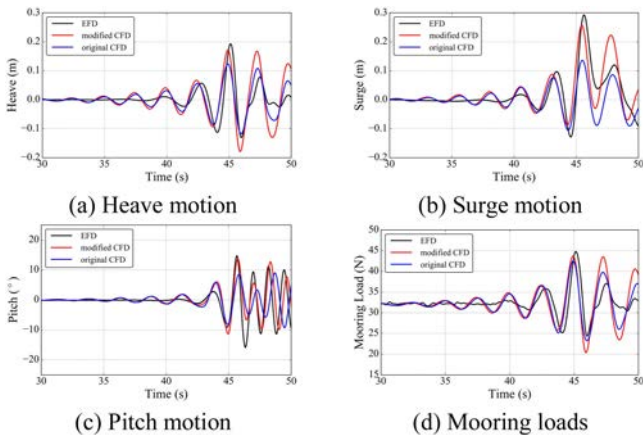


Fig. 8 Time histories of buoy motion and mooring load for case 1BT3

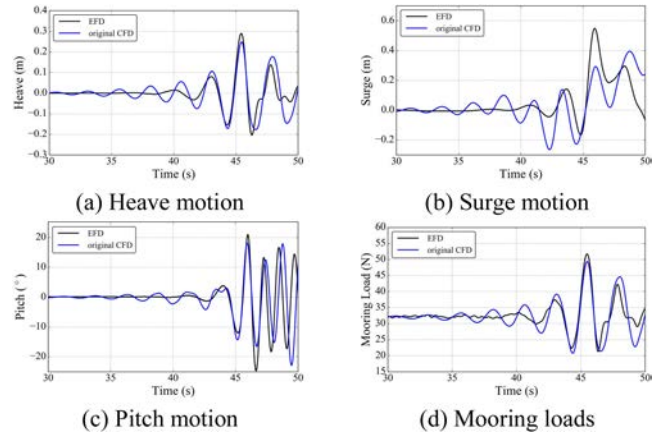


Fig. 9 Time histories of buoy motion and mooring load for case 2BT3

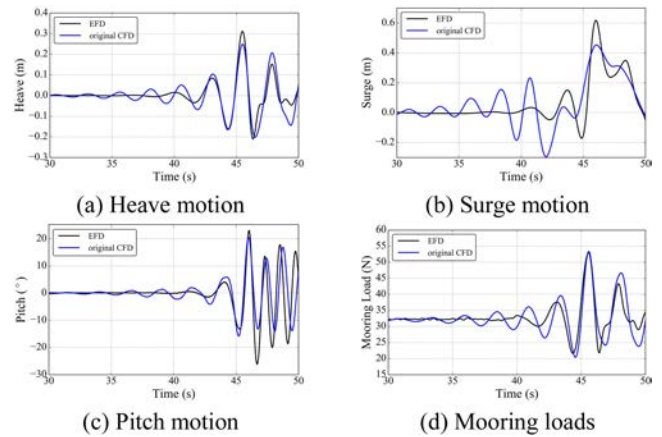


Fig. 10 Time histories of buoy motion and mooring load for case 3BT3

but also changed the phase of the motion. For surge motion, the effect of wave steepness is more obvious. The difference of surge motion for 2BT3 and 3BT3 shows larger disparity than the wave steepness.

Figure 12 shows a series of snapshots of the free surface around the buoy for case 1BT3, while Fig. 13 shows the distribution of the velocity vector around the buoy at the same time intervals. When the wave encounters the buoy, the buoy moves in heave, surge, and pitch with relatively large amplitude. This may have

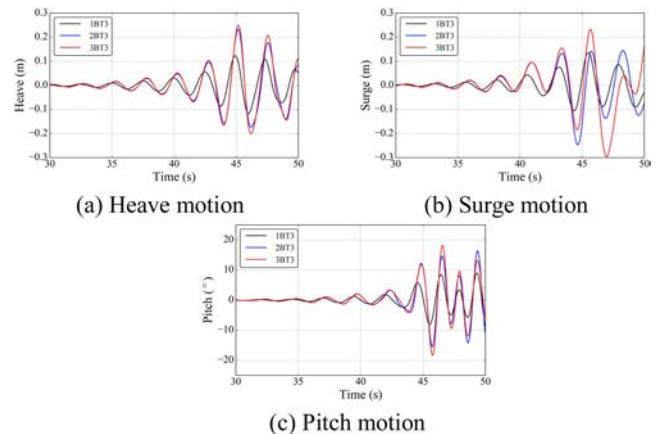


Fig. 11 Time history of the motion response of the buoy under different wave steepnesses

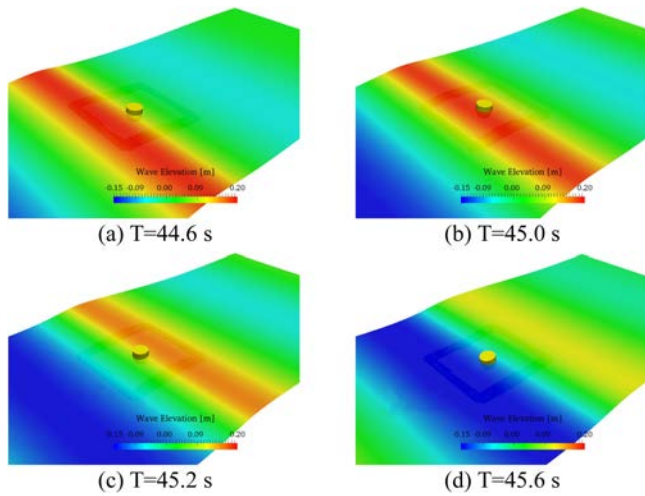


Fig. 12 Snapshots of the free surface around the buoy during the interaction for case 1BT3

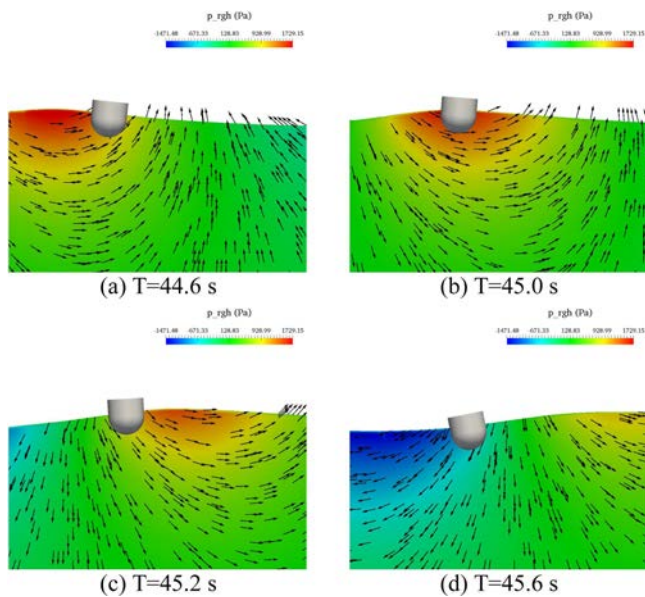


Fig. 13 Distribution of velocity vector around the buoy during the interaction for case 1BT3

great influence on mooring loads. When the wave crest passes by the buoy, the wave runs up at the shoulder of the buoy (at  $T = 45.2$  s). When the trough approaches the buoy, an obvious wave diffraction can be found in front of the buoy.

Figure 14 shows a series of snapshots of the free surface around the buoy for case 2BT3, while Fig. 15 shows the distribution of the velocity vector around the buoy at the same time intervals. As the wave steepness increases, the time of the wave diffraction around the buoy is advanced compared to the case of a smaller wave steepness. The obvious runup and wave breaking can be seen in the front of the buoy at  $T = 45.0$  s. Furthermore, the wave runup appears at the rear of the buoy after the wave crest passes by the buoy.

CONCLUSIONS

The present work is part of the comparative study on focused wave interactions with moored floating structures from the CCP-WSI working group. This paper applied the CFD solver naoe-

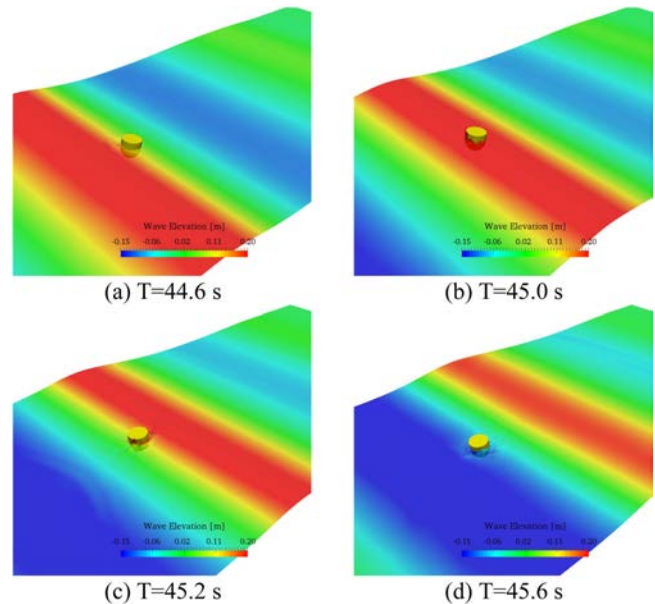


Fig. 14 Snapshots of the free surface around the buoy during the interaction for case 2BT3

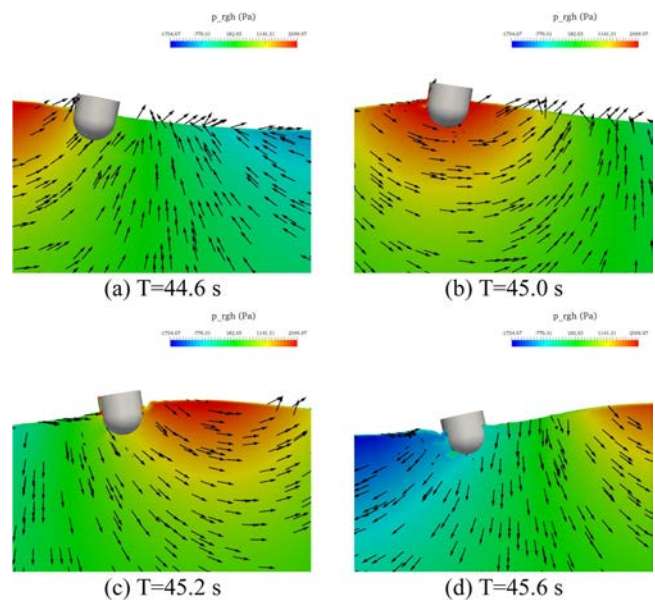


Fig. 15 Distribution of the velocity vector around the buoy during the interaction for case 2BT3

FOAM-SJTU to simulate the interaction between a focused wave and a hemispherical-bottomed buoy. First, the crest-focused waves with three different steepnesses in an empty wave tank are simulated. The time history of the focused wave at several locations was compared with the experimental data provided by CCP-WSI working group. The results indicate that the focused wave in experiment is well reproduced by the naoe-FOAM-SJTU solver, although the oscillation of the surface before and after the largest crest is more evident than the experimental results. This may be a result of the effect of the slope in the front of the tank. Then a moored hemispherical-bottomed buoy is placed at the focused location in the numerical wave tank. The buoy’s heave and surge displacement, pitch angle, and mooring load are presented and compared against corresponding physical data. The results indicate that our CFD solver can provide relatively good agreement

with the experimental data in heave and pitch motion. The mooring loads also show great consistency with the experimental data. Although surge displacement cannot be predicted accurately, the long-period surge oscillation still can be captured in our numerical simulations. Further work to improve the accuracy of motion and load prediction should be focused on the new boundary condition for the NewWave theory and the application of overset grid technology.

## ACKNOWLEDGEMENTS

This work was supported by the National Natural Science Foundation of China (51879159), National Key Research and Development Program of China (2019YFB1704204), Chang Jiang Scholars Program (T2014099), Shanghai Excellent Academic Leaders Program (17XD1402300), Innovative Special Project of the Numerical Tank of Ministry of Industry and Information Technology of China (2016–23/09), and Lloyd's Register Foundation for the doctoral student, for which the authors are most grateful.

## REFERENCES

- Bharath, A, Penesis, I, Nader, JR, and Macfarlane, G (2016). "Non-Linear CFD Modelling of a Submerged Sphere Wave Energy Converter," *Proc 3rd Asian Wave Tidal Energy Conf*, Singapore, AWTEC, 320–329.
- Bredmose, H, and Jacobsen, NG (2010). "Breaking Wave Impacts on Offshore Wind Turbine Foundations: Focused Wave Groups and CFD," *Proc 29th Int Conf Offshore Mech Arct Eng*, Shanghai, China, ASME, 3, 397–404. <https://doi.org/10.1115/OMAE2010-20368>.
- Coe, RG, and Neary, VS (2014). "Review of Methods for Modeling Wave Energy Converter Survival in Extreme Sea States," *Proc 2nd Mar Energy Technol Symp*, Seattle, WA, USA, METS, 1–8.
- Goteman, M, et al. (2015). "Wave Loads on a Point-Absorbing Wave Energy Device in Extreme Waves," *J Ocean Wind Energy*, 2(3), 176–181. <https://doi.org/10.17736/jowe.2015.mkr03>.
- Hann, M, Greaves, D, and Raby, A (2015). "Snatch Loading of a Single Taut Moored Floating Wave Energy Converter Due to Focused Wave Groups," *Ocean Eng*, 96, 258–271. <https://doi.org/10.1016/j.oceaneng.2014.11.011>.
- Hirt, CW, and Nichols, BD (1981). "Volume of Fluid (VOF) Method for the Dynamics of Free Boundaries," *J Comput Phys*, 39, 201–225. [https://doi.org/10.1016/0021-9991\(81\)90145-5](https://doi.org/10.1016/0021-9991(81)90145-5).
- Li, Y, and Lin, M (2012). "Regular and Irregular Wave Impacts on Floating Body," *Ocean Eng*, 42, 93–101. <https://doi.org/10.1016/j.oceaneng.2012.01.019>.
- Lim, H, Manuel, L, and Low, YM (2018). "On Efficient Long-Term Extreme Response Estimation for a Moored Floating Structure," *Proc 37th Int Conf Offshore Mech Arct Eng*, Madrid, Spain, ASME, 3, V003T02A043–V003T02A049. <https://doi.org/10.1115/OMAE2018-78763>.
- Lou, J (2017). *Numerical Simulation, Laboratory and Field Experiments, Analysis and Design of Wave Energy Converter and Mooring System*, PhD Thesis, Oregon State University, Corvallis, OR, USA.
- Mai, T, Greaves, D, Raby, A, and Taylor, PH (2016). "Physical Modelling of Wave Scattering Around Fixed FPSO-Shaped Bodies," *Appl Ocean Res*, 61, 115–129. <https://doi.org/10.1016/j.apor.2016.10.007>.
- Palm, J, Eskilsson, C, Bergdahl, L, and Bensow, R (2018). "Assessment of Scale Effects, Viscous Forces and Induced Drag on a Point-Absorbing Wave Energy Converter by CFD Simulations," *J Mar Sci Eng*, 6(4), 124. <https://doi.org/10.3390/jmse6040124>.
- Palm, J, Eskilsson, C, Paredes, GM, and Bergdahl, L (2013). "CFD Simulation of a Moored Floating Wave Energy Converter," *Proc 10th Eur Wave Tidal Energy Conf*, Aalborg, Denmark, 25.
- Palm, J, Eskilsson, C, Paredes, GM, and Bergdahl, L (2016). "Coupled Mooring Analysis for Floating Wave Energy Converters Using CFD: Formulation and Validation," *Int J Mar Energy*, 16, 83–99. <https://doi.org/10.1016/j.ijome.2016.05.003>.
- Ransley, E (2015). *Survivability of Wave Energy Converter and Mooring Coupled System Using CFD*, PhD Thesis, University of Plymouth, Plymouth, UK.
- Ransley, EJ, Greaves, D, Raby, A, Simmonds, D, and Hann, M (2017). "Survivability of Wave Energy Converters Using CFD," *Renewable Energy*, 109, 235–247. <https://doi.org/10.1016/j.renene.2017.03.003>.
- Roache, PJ (1994). "Perspective: A Method for Uniform Reporting of Grid Refinement Studies," *J Fluids Eng*, 116(3), 405–413. <https://doi.org/10.1115/1.2910291>.
- Savin, A, Svensson, O, and Leijon, M (2012). "Azimuth-Inclination Angles and Snatch Load on a Tight Mooring System," *Ocean Eng*, 40, 40–49. <https://doi.org/10.1016/j.oceaneng.2011.12.007>.
- Shen, ZR, Wan, DC, and Carrica, PM (2015). "Dynamic Overset Grids in OpenFOAM with Application to KCS Self-Propulsion and Maneuvering," *Ocean Eng*, 108, 287–306. <https://doi.org/10.1016/j.oceaneng.2015.07.035>.
- Stern, F, Wilson, R, and Shao, J (2006). "Quantitative V&V of CFD Simulations and Certification of CFD Codes," *Int J Numer Methods Fluids*, 50(11), 1335–1355. <https://doi.org/10.1002/flid.1090>.
- Sykes, RK, Lewis, AW, and Thomas, GP (2009). "A Hydrodynamic Study of a Floating Circular OWC," *Proc 8th Eur Wave Tidal Energy Conf*, Uppsala, Sweden, 618–627.
- Wagner, JJ, Wagner, JR, and Hayatdavoodi, M (2016). "Hydrodynamic Analysis of a Submerged Wave Energy Converter," *Proc 4th Mar Energy Technol Symp*, Washington, DC, USA, METS, 25–27.
- Wang, JH, Liu, XJ, and Wan, DC (2015). "Numerical Simulation of an Oblique Towed Ship by naoe-FOAM-SJTU Solver," *Proc 25th Int Ocean Polar Eng Conf*, Kona, HI, USA, ISOPE, 3, 432–438.
- Wang, JH, Liu, XJ, and Wan, DC (2016). "Numerical Prediction of KCS Self-Propulsion in Shallow Water," *Proc 26th Int Ocean Polar Eng Conf*, Rhodes, Greece, ISOPE, 4, 757–763.
- Wang, JH, and Wan, DC (2016). "Numerical Simulation of Pure Yaw Motion Using Dynamic Overset Grid Technology," *Chin J Hydrodyn*, 31(5), 567–574. <https://doi.org/10.16076/j.cnki.cjhd.2016.05.006>.
- Wang, JH, and Wan, DC (2018). "CFD Investigations of Ship Maneuvering in Waves Using naoe-FOAM-SJTU Solver," *J Mar Sci Appl*, 17(3), 443–458. <https://doi.org/10.1007/s11804-018-0042-4>.
- Wang, JH, Zhao, WW, and Wan, DC (2019). "Development of naoe-FOAM-SJTU Solver Based on OpenFOAM for Marine Hydrodynamics," *J Hydrodyn*, 31(1), 1–20. <https://doi.org/10.1007/s42241-019-0020-6>.

Westphalen, J (2011). *Extreme Wave Loading on Offshore Wave Energy Devices Using CFD*, PhD Thesis, University of Plymouth, Plymouth, UK.

Wolgamot, HA, and Fitzgerald, CJ (2015). “Nonlinear Hydrodynamic and Real Fluid Effects on Wave Energy Converters,” *J Power Energy*, 229(7), 772–794.  
<https://doi.org/10.1177/0957650915570351>.

Zhao, WW, and Wan, DC (2016). “Numerical Study of 3-D Flow Past a Circular Cylinder at Subcritical Reynolds Number Using SST-DES and SST-URANS,” *Chin J Hydrodyn*, 31(1), 1–8.  
<https://doi.org/10.16076/j.cnki.cjhd.2016.01.001>.

Zhao, WW, Wan, DC, and Hu, ZQ (2018). “Numerical Investigation of Vortex-Induced Motions of a Paired-Column Semisubmersible in Currents,” *Ocean Eng*, 164, 272–283.  
<https://doi.org/10.1016/j.oceaneng.2018.06.023>.

***The Proceedings of  
The Twenty-ninth (2019) International  
Ocean and Polar Engineering Conference  
Honolulu, June 16–21, 2019***

ISBN 978–1–880653–85–2      ISSN 1098–6189

Indexed by Web of Science, Google Scholar, EI (Compendex), Scopus, Fluidex and others.

**VOLUME I**

**The 14th OCEAN MINING AND GAS HYDRATES SYMPOSIUM**

Gas Hydrates, Deep Ocean Mining, Exploration, Environment  
**RENEWABLE ENERGY: OFFSHORE WIND AND OCEAN**

Wave Energy, Offshore Wind Structures, Floating Wind Structures, Offshore Wind Turbine and Energy, Tidal and Current Turbine and Energy, Energy Storage

**OCEAN, ARCTIC ENVIRONMENT AND ECOSYSTEM**

Oil Spill, Emission, Ecosystem, Water Quality

**ARCTIC SCIENCE AND TECHNOLOGY**

Russian Arctic Ice, Ice Properties, Ice Kinematics, Ice Loads, Arctic Ship Design, Ice Navigation, Arctic Shipping, Ice Management and Dynamic Positioning, Emergency and Remote Sensing

**ARTIFICIAL INTELLIGENCE, MACHINE LEARNING, DIGITALIZATION, NEURAL NETWORK**

**LNG, OFFSHORE MECHANICS, OCEAN TECHNOLOGY**

Installation, Jackup and Jacket Design and Installation, Floating Dynamics and Operation, LNG System and Bunkering, Structural Health Monitoring (SHM), Deepwater Drilling

**UNDERWATER TECHNOLOGY**

Underwater Sensing and Navigation, Underwater Dynamics, Control and Design

**VOLUME II**

**SUBSEA, PIPELINES, RISERS AND UMBILICALS**

Pipeline Mechanics, Design and Manufacturing, Riser Mechanics and Design, Subsea Umbilicals, Multiphase Flows, Subsea Installation and Pipeline Mechanics

**GEOTECHNICAL ENGINEERING**

Spudcan, Pile Foundation, Suction Bucket Foundation, Offshore Foundation, Soil Characterization, Simulation and Experiment, Site Characterization, Soil-Pipeline Interactions, Ground Improvement

**VOLUME III**

**HYDRODYNAMICS**

Wave Mechanics, MetOcean, Storm Surge, Flooding, Hydrodynamic Loads and Responses, CFD Hydrodynamics of Ship and FPSO Impact, Dynamic Positioning, CCP-WSI Blind Tests, Floating Tunnel

**TSUNAMI AND SAFETY SYMPOSIUM**

**SLOSHING DYNAMICS AND DESIGN**

**VORTEX-INDUCED VIBRATIONS (FIV, VIV)**

**COASTAL HYDRODYNAMICS**

Coastal Wave Mechanics, Tide and Estuary, Waves on Structures and Responses, Storm Surge and Protection, Sediment Transport, Coastal Erosion and Management

**VOLUME IV**

**HIGH-PERFORMANCE MATERIALS (HPM)**

Advances in Materials, Low-Temperature, Cryogenic Materials, Advance in Welding Technology, Fatigue and Fracture, Asset Integrity, Additive Manufacturing (3D Printing), Hydrogen Embrittlement Fundamentals

**MECHANICS, HYDROELASTICITY, IMPACT,**

**COLLISION, RISK**

Hydroelasticity, Impact, Collision, Risk Analysis, Buckling and Vibration

**ADVANCED SHIP TECHNOLOGY**

EEDI, Added Resistance, Ship Resistance, Ship Navigation and Maneuvering, Ship Powering, Propulsor, Performance, Cavitation, Ship Structure and Strength, Ship Design and Production, Ship Stability, Squat and Safety